Chinese Chemical Letters 35 (2024) 108898

Contents lists available at ScienceDirect

Chinese Chemical Letters

journal homepage: www.elsevier.com/locate/cclet

In situ sulfur-doped mesoporous tungsten oxides for gas sensing toward benzene series

Yu Deng[a,b,e,1], Yan Liu[b,1], Yonghui Deng[b], Jinsheng Cheng[d], Yidong Zou[c,*], Wei Luo[a,*]

[a] State Key Laboratory for Modification of Chemical Fibers and Polymer Materials, College of Materials Science and Engineering, Donghua University, Shanghai 201620, China
[b] Department of Chemistry, State Key Laboratory of Molecular Engineering of Polymers, Shanghai Key Laboratory of Molecular Catalysis and Innovative Materials, iChEM, Fudan University, Shanghai 200433, China
[c] Department of Polymeric Materials, School of Materials Science and Engineering, Tongji University, Shanghai 201804, China
[d] Henry-Fork School of Food Sciences, Shaoguan University, Shaoguan 512005, China
[e] State Key Lab of Transducer Technology, Shanghai Institute of Microsystem and Information Technology, Chinese Academy of Sciences, Shanghai 200050, China

ARTICLE INFO

Article history:
Received 12 June 2023
Revised 27 July 2023
Accepted 5 August 2023
Available online 10 August 2023

Keywords:
Mesoporous materials
Benzene series
Tungsten oxides
Sulfur doping
Gas sensor

ABSTRACT

Benzene series as highly toxic gases have inevitably entered human life and produce great threat to human health and ecological environment, and thus it is distinctly meaningful to monitor benzene series with quickly, real-time and efficient technique. Herein, novel sulfur-doped mesoporous WO_3 materials were synthesized via classical *in-situ* solvent evaporation induced co-assembly strategy combined with doping engineering, which possessed highly crystallized frameworks, high specific surface area (40.9–63.8 m^2/g) and uniform pore size (~18 nm). Benefitting from abundant oxygen vacancy and defects *via* S-doping, the tailored mesoporous S/mWO_3 exhibited excellent benzene sensing performance, including high sensitivity (50 ppm *vs.* 48), low detection limit (*ca.* 500 ppb), outstanding selectivity and favorable stability. In addition, the reduction of band gap resulted from S-doping promotes the carrier migration in the sensing materials and the reaction at the gas–solid sensing interfaces. It provides brand-new approach to design sensitive materials with multiple reaction sites.

In recent years, with the proposed concept of sustainable development, air quality and environmental problem has attracted more and more attention. In general, the air quality can be influenced by various harmful gases (*e.g.*, CO, NO, NO_2, SO_2) and organic volatile gases that are not easy to perceive, such as formaldehyde, acetone, benzene and toluene [1–3]. Benzene and its derivatives volatile organic compounds (VOCs) have been widely recognized as strong carcinogens by the World Health Organization. In addition, short-term exposure can cause headache, allergy and dyspnea, while long-term exposure can lead to all kinds of cancer and leukemia. Therefore, it is extremely important to realize a rapid and convenient detection of the benzene series by using gas sensors based on various sensitive materials [4,5].

By contrast, semiconductor metal oxides (SMOs) gas sensors have unique advantages for VOCs monitoring applications because they can realize highly sensitive and stable gas sensing response with a low manufacturing and application cost, which are suitable for miniaturization and integration with other devices [6,7]. However, the comprehensive property of the existed SMOs gas sensors usually endowed weak selectivity due to lacking of efficient regulating of the microstructures and the gas–solid interfacial property for sensing reaction [8–10]. Numerous studies have demonstrated that porous SMOs could provide high specific surface area and abundant active sites for enhancing sensitivity of gas sensors [11–13]. The gas sensing selectivity is directly relevant with the adsorption, catalytic conversion of target gas molecules, and therefore, considerable efforts have been devoted to modifying SMOs framework *via* loading noble metal nanoparticles [14–16] and/or doping with heteroatoms [17–19]. In contrast, transition metal element doping is a commonly used method in exploiting high-efficient catalysts, energy materials and sensing materials. Introducing additional transition metal atoms into the metal oxide framework can regulate the energy band structure, electronic structure and chemical microenvironments (*e.g.*, surface acidity, polarity) of materials. In addition, it can also increase defect density, active sites and the content of oxygen vacancy [20–22], which is favorable for many applications such as catalysis, and chemical sensing.

* Corresponding authors.
E-mail addresses: ydzou@tongji.edu.cn (Y. Zou), wluo@dhu.edu.cn (W. Luo).
[1] These authors contributed equally to this work.

https://doi.org/10.1016/j.cclet.2023.108898
1001-8417/

Except for metal element doping, non-metallic element doping was also widely studied to tune the materials' properties *via* either gas–solid interface reaction or wet chemical synthesis [23–25]. Various guest heteroatoms such as non-metallic elements B [26], C [27], N [28], S [29], P [30], have been employed to dope host metal oxides to regulate their ionic conductivity, reduce the recombination rate of carriers and enhance materials performance [31–35]. Appropriate doping with non-metallic elements can increase the conductivity by adjusting the band gap structure, improve the mobility of carriers, and increase the content of defects and oxygen vacancies [36]. Based on these considerations, it is expected that the rational construction of porous structure and heteroatom doped framework is a promising strategy to develop high-performance sensitive materials for gas sensing applications.

Herein, a multi-component co-assembly method was employed to straightforward synthesize mesoporous tungsten oxides (mWO_3) with *in-situ* S-doped crystalline framework. The obtained S-doped mWO_3 (denoted as S/mWO_3) possess unique mesoporous structure, high specific surface area (40.9–63.8 m^2/g) and uniform pore size (~18 nm). Due to the abundant oxygen vacancies and internal defects generated by S-doping effect, the S/mWO_3 materials showed ultrahigh sensitivity toward low-concentration benzene at 250 °C (50 ppm *vs.* 48), which is about five times higher than that in pure mWO_3. In addition, the sensor has excellent cycle stability, rapid response rate (only 10 s) and excellent selectivity toward benzene series (*e.g.*, benzene and toluene). Interestingly, there was a significant response change even when the benzene concentration was reduced to 500 ppb, which exhibited great application potential in ultra-low concentration monitoring, such as industrial safety production. The enhanced gas sensing performance was attributed to the significantly increased defect concentration and oxygen vacancy content, which was caused by the introduction of sulfur and the loss during calcination. At the same time, the reduction of band gap further promotes the carrier migration in the sensing materials and the reaction at the gas–solid sensing interfaces.

In this study, facile multi-component co-assembly strategy was employed to synthesize mesoporous S-doped WO_3 based on PEO_{114}-*b*-PS_{315} (M_n = 37,729 g/mol, PDI = 1.22) as the structure directing agent. In addition, bifunctional small molecule 4-hydroxyphenylthiophenol as the sulfur source, anhydrous tungsten chloride is used as the W source, and acetylacetone is added into the assembly system as the chelating agent to inhibit the excessive hydrolysis of W ion in the co-assembly behavior (Scheme 1). During the assembly process, these organic–inorganic components can cooperate with each other to form spherical composite micelles *via* weak interactions such as hydrogen bonds and coordination bonds. As the evaporation of tetrahydrofuran (THF), the formed spherical micelles can accumulate into uniform mesoscopic structure, and the obtained organic–inorganic mesoporous composite is further calcined and crystallized in nitrogen atmosphere. It is worth noting that the 4-hydroxyphenylthiophenol plays an important role in induced assembly and doping engineering. It can connect with the hydrophilic PEO segments through hydrogen bond, and the partially hydrolyzed W^{6+} complexed by acetylacetone can coordinate with the hydrophilic segments. The soft template is carbonized into amorphous sp^2-hybrid carbon to support the framework structure. Finally, the crystallized S/mWO_3 materials were obtained after removing the residual carbon by calcination in air.

By changing the feeding amount of S:WO_3, a series of S-doped WO_3 samples (denoted as S/mWO_3-*X*, herein *X* represents different feed mass ratios S: WO_3 = 0, 2, 5, 10 wt%) were obtained. It can be seen that the obtained mWO_3 and S/mWO_3-5 can maintain well mesoporous structure and high porosity (Figs. 1a–e). In the high-power transmission electron microscope, it can see that the pore size is about 20 nm. In addition, according to the selected

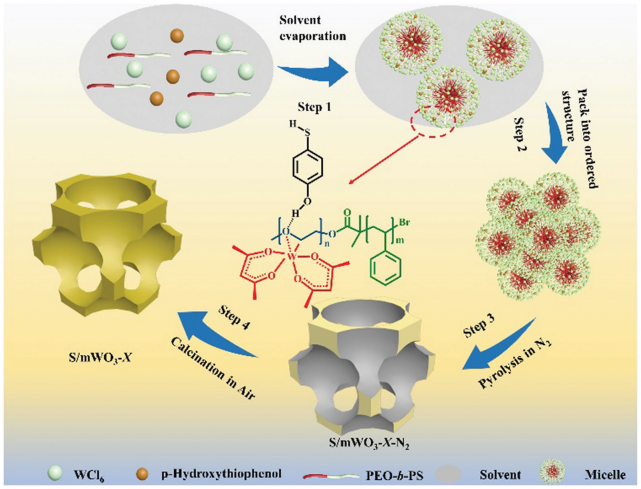

Scheme 1. The synthesis of S-doped mesoporous WO_3, Step 1, the co-assembly of amphiphilic copolymers, organic additives and inorganic precursor into composite micelles with the evaporation of THF; Step 2, composite micelles packed into mesostructured composites; Step 3, pyrolysis treatment of the organic–inorganic composites at different temperatures; Step 4, calcination treatment in air to remove the residual carbon, yielding S-doped mesoporous WO_3.

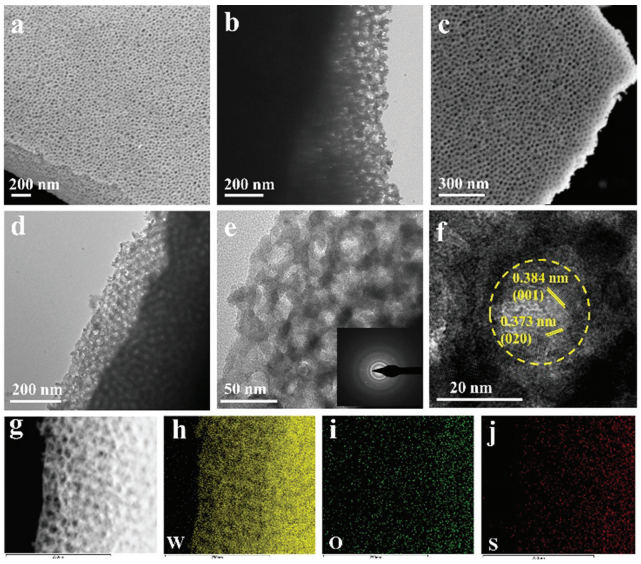

Fig. 1. SEM and TEM images of (a, b) mWO_3 and (c–e) S/mWO_3-5, (f) HRTEM image of S/mWO_3-5, (g) STEM and element images of S/mWO_3-5, (h) W element, (i) O element, (j) S element. The inset of (e) is the corresponding SAED image (Scale bar: 250 nm).

area electron diffraction (SAED) diagram (inset of Fig. 1e), it shows that the diffraction diagram is composed of polycrystalline diffraction rings, indicating that the pore wall of the material is mainly composed of polycrystalline nanoparticles, which can be also seen in the high-resolution transmission electron microscope (HRTEM) (Fig. 1f). Especially, the pore wall structure of S/mWO_3-5 is basically formed by the accumulation of WO_3 grains, in which the exposed lattice stripes of 0.384 nm and 0.373 nm are corresponding to the (001) and (020) crystal planes of WO_3, respectively. Scanning transmission electron microscope (STEM) can clearly see the mesoporous structure (Fig. 1g), and the element distribution diagram (Figs. 1h–j) can clearly show that all elements are homogeneously distributed in the pore frameworks. Furthermore, other S/mWO_3-*X* with various doping ratios also show that the mesoporous structure can be effectively maintained (Fig. S1 in Supporting information).

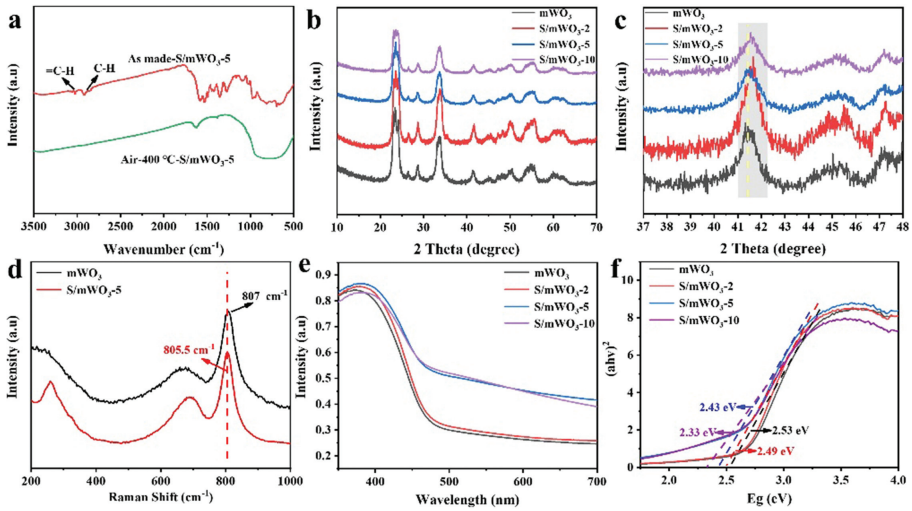

Fig. 2. (a) FTIR spectra of as made S/mWO$_3$-5 and S/mWO$_3$-5, (b, c) XRD pattern of S/mWO$_3$-*X*, (d) Raman spectra of mWO$_3$ and S/mWO$_3$-5, (e) UV–vis spectra and (f) plot of $(ahv)^2$ of S/mWO$_3$-*X* (X = 0, 2, 5, 10).

Fourier transform infrared spectroscopy (FTIR) is used to characterize the component information in the process of material synthesis. Taking S/mWO$_3$-5 as an example, it can be seen that the absorption vibration peak of organic matter can be clearly seen in the characterization of the sample before calcination (Fig. 2a). The peaks at 2917 and 3028 cm^{-1} are corresponded to the stretching vibration peaks of C–H and -C=H in the soft template respectively. It is found that these two peaks disappear in the characterization of the sample after calcination under air conditions, implying the removal of organic template [37]. The XRD peaks of all S/mWO$_3$-*x* samples showed high crystallinity (Fig. 2b), corresponding to the crystalline orthorhombic WO$_3$ phase (PDF#20-1324) [38]. However, there was no obvious WS$_2$ peak, and it was mainly because the doping content of sulfur was not high enough. In addition, in the calcination process, a certain content of S was easy to be lost under high temperature, so only a small amount of S could be preserved, and some of the lost S vacancies would exist in the form of defects. It can be seen from the local enlarged picture of XRD (Fig. 2c) that the peak at about 42° shifts to a high angle to a certain extent, indicating that a certain amount of S element is successfully doped into the WO$_3$ lattice [39]. Furthermore, it is also proved by Raman spectroscopy (Fig. 2d) that after the introduction of S element, the W–O stretching vibration peak of about 807 cm^{-1} shifts to a certain extent. Compared with pure mWO$_3$, the W–O stretching vibration peak of S/mWO$_3$-5 shifts to a lower angle from 807 cm^{-1} to 805.5 cm^{-1}, which is due to the lattice distortion caused by the doping of S atoms with different radii, and it is consistent with the results of XRD, indicating that S atoms are successfully doped into the lattice of WO$_3$ [17,19]. Many researchers have proved that sulfur doping can regulate the band gap width of SMOs, reduce the recombination rate of electron holes and improve the catalytic and sensing performance [40–43]. For the change of the band gap width of the material before and after doping, the analysis of the solid-state UV spectrum shows that compared with the undoped mWO$_3$ (Figs. 2e and f), the absorption spectra of the S/mWO$_3$-*X* materials are red shifted, and the corresponding band gap width is reduced from the initial 2.53 eV to 2.33 eV. It indicates that after the introduction of sulfur element, the band gap width is reduced, which is conducive to the migration of carriers. The narrower band gap of S/mWO$_3$-*X* is originated from the decreased energy difference between the maximum valence band and the Fermi level, and combined with the lower conduction band [32,40].

The valence states of elements in the materials were analyzed by XPS spectrum. The peaks at 530.3 eV and 531.0 eV of O 1s are corresponding to lattice oxygen and adsorbed oxygen (O^- and O^{2-}), respectively (Figs. 3a and d). In contrast, the position of O 1s peak of S/mWO$_3$-5 shifts to the direction of low binding energy (530.1 and 530.8 eV), which is caused by the change of chemical environment around O atoms caused by S atoms. In addition, the distribution of oxygen species obtained before and after doping is obtained (Table S1 in Supporting information). After the introduction of S element, the adsorbed oxygen content increases from 33.5% to 36.8%. High adsorbed oxygen content will promote the surface gas catalytic reaction. W 4f XPS spectrum (Figs. 3b and e) shows that both W^{5+} and W^{6+} exist in the materials. After the introduction of sulfur, the content of W^{5+} increases significantly [38], indicating that more defects are formed after S doping. Analyze the XPS spectrum of S 2p of the tested samples after N_2 and air calcination respectively, it can be seen that compared with the S 2p peak of the samples after N_2 calcination (Figs. 3c and f), the S 2p peak after air calcination is significantly weakened because the S element is easy to be lost at high temperature. Especially the S element on the pore walls, while XPS mainly tests the component information with a thickness of about 10 nm, so it is difficult to detect the S element. The peak of 162 eV corresponds to the peak of S^{2-}, while 168 and 170 eV are assigned to SO_x^{2-}, because S element can replace O position and combine with W to form a small amount of WS$_2$. At the same time, some S atoms combine with O atoms in the form of interstitial doping are oxidized, and the valence state increases. Comparing the samples calcined in N_2 and air, it can be seen that after air calcination, a part of S element in the material will be lost and produce defects. The generated defects are easy to adsorb oxygen molecules and the content of adsorbed oxygen on the surface will increase. For the analysis of the mesoporous structure of mWO$_3$, it can be seen that the obtained mesoporous S/mWO$_3$-*X* has high specific surface area (40.9–63.8 m^2/g) (Fig. S2 and Table S2 in Supporting information) and uniform pore size (18 nm). Therefore, it can be seen that S doping will not damage the mesoporous structure.

In general, high specific surface area and connectivity will be conducive to gas molecule transmission and gas–solid interface reaction, increase surface active sites for the adsorption of oxygen molecules and target gas molecules, and improve the utilization rate of internal materials. At the same time, the unique Knudsen diffusion of mesoporous materials can increase the contact frequency between gas molecules and materials, which is benefit to the improvement of gas sensing performance [44–46]. During the sensing test, the working temperature has a great influence on

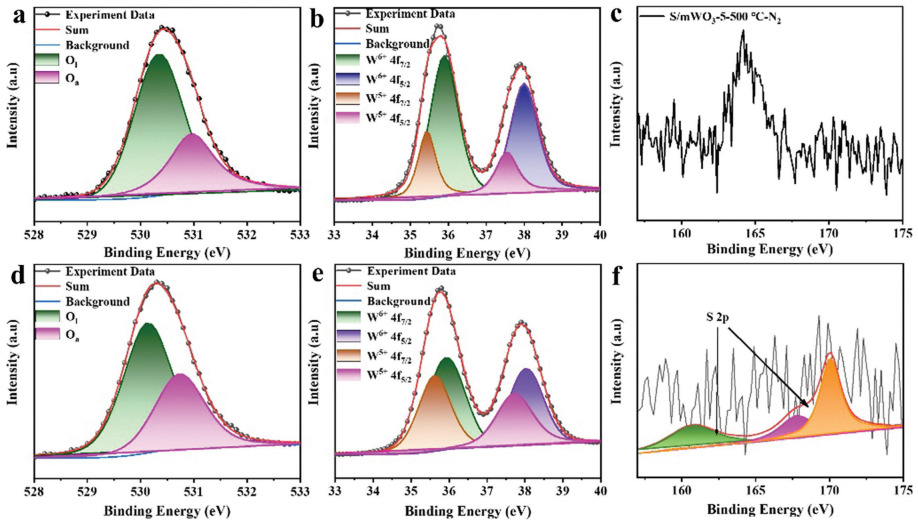

Fig. 3. XPS spectra of mWO$_3$: (a) O 1s, (b) W 4f; XPS spectra of S/mWO$_3$-5: (d) O 1s, (e) W 4f, S 2p of S/mWO$_3$-5 pyrolysis in (c) N_2 and (f) calcination in air.

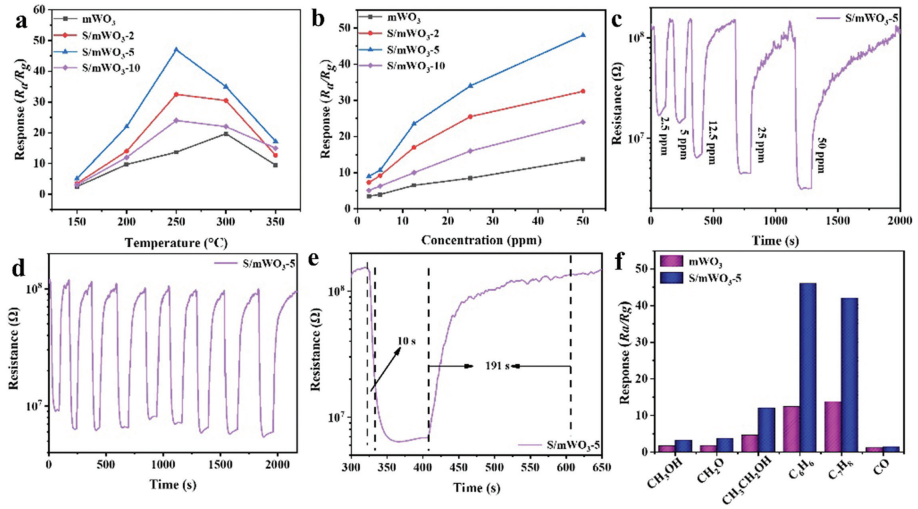

Fig. 4. (a) Sensing response of S/mWO$_3$-*X* at various temperature to 50 ppm benzene. (b) Sensing response of S/mWO$_3$-*X* to various concentration of benzene at 250 °C. (c) The dynamic curve of S/mWO$_3$-5 at 250 °C. (d) The repeat test of S/mWO$_3$-5 to 12.5 ppm benzene at 250 °C. (e) The response and recovery time of S/mWO$_3$-5 to 12.5 ppm benzene at 250 °C. (f) Sensing selectivity of mWO$_3$ and S/mWO$_3$-5 to 50 ppm gasses.

the response and selectivity of gas sensing, so it is necessary to determine the optimal working temperature of gas sensing reaction. The temperature test range is 150–350 °C, and the response to 50 ppm benzene gas increases first and then decreases. This is mainly because the increase of working temperature can provide more energy for surface adsorption/catalytic reaction between targeted gas molecules and sensitive materials, and in addition it can reduce the activation energy of surface reaction. However, the excessive increase of working temperature will accelerate the desorption process of gas molecules, which is not conducive to the adsorption of gas molecules, so it is not conducive to further optimizing the gas sensing performance. After S doping, the working temperature is reduced, mainly by increasing the content of adsorbed oxygen on the surface and reducing the activation energy of surface reaction, so that the optimal working temperature is reduced from 300 °C to 250 °C (Fig. 4a). In addition, S/mWO$_3$-5 shows the best sensing response to benzene (50 ppm *vs.* 48). For different concentrations, the gas sensing response gradually increases with the increase of concentration (Fig. 4b). In terms of S/mWO$_3$-5, the corresponding response of benzene concentration increased from 9 (2.5 ppm) to 48 (50 ppm), which is much higher than the response value of mWO$_3$ (2.5 ppm: 3.5, 50 ppm: 13.7). The improvement of gas sensing performance is due to the increase of internal defects and oxygen vacancy content after the addition of S atoms, which promotes the surface catalytic reaction. The response–recovery curve of S/mWO$_3$-*X* (X = 0, 2, 5, 10) also demonstrated that these sensors possess high sensitivity (Fig. 4c and Fig. S3 in Supporting information).

In practical application, the detection of low concentration benzene is very important for the safety forewarning. The prepared S/mWO$_3$-*X* materials can still maintain excellent gas sensing performance for low concentration benzene (1.5 *vs.* 500 ppb) (Fig. S4 in Supporting information). In addition, S/mWO$_3$-5 shows excellent cycle stability toward 12.5 ppm benzene (Fig. 4d). In nine cycle testing, the change of equilibrium resistance is less than 10%, indicating that the materials have good stability. At the same time, the cyclic test resistance of S/mWO$_3$-5 basically remained unchanged after one week test, indicating that the device could still maintain a relatively stable response value (Fig. S5 in Supporting information). In order to deal with complex environmental gases and identify specific gases timely and accurately, excellent selectivity is required. As shown in Fig. 4f, it exhibited excellent gas sensi-

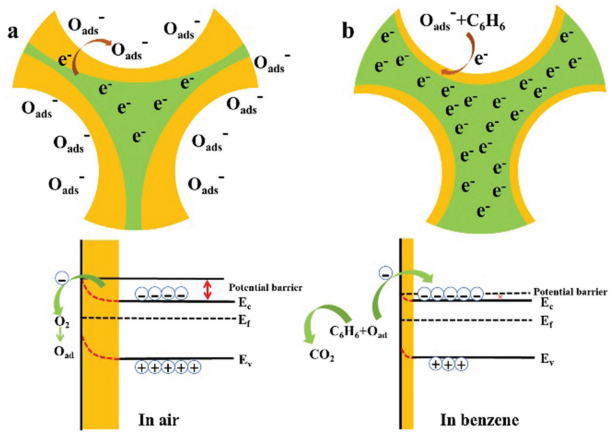

Scheme 2. The sensing mechanism of S/mWO$_3$-*X*, the energy band structure and electron transfer process of S/mWO$_3$-*X*, (a) in air and (b) in benzene.

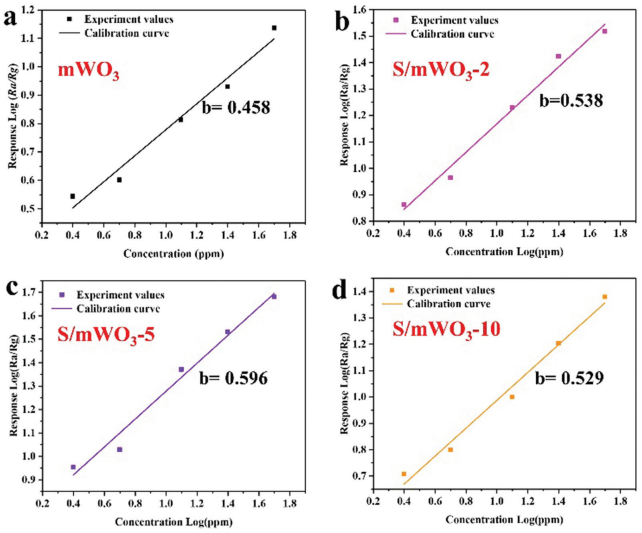

Fig. 5. Calibration curves of response *versus* benzene concentration of S/mWO$_3$-*X* in the range of 2.5–50 ppm, (a) mWO$_3$, (b) S/mWO$_3$-2, (c) S/mWO$_3$-5 and (d) mWO$_3$-10.

tivity to benzene and toluene, which could be significantly different from other interfering gases (such as methanol, formaldehyde, ethanol and CO). The response value of S/mWO$_3$-5 to 50 ppm benzene and toluene is about 4 times higher than that of interfering gases, indicating that it has excellent selectivity toward benzene series. In addition, the speed of response and recovery is also one of the evaluation criteria of gas sensor. The response–recovery curve of S/mWO$_3$-5 to 12.5 ppm benzene showed a faster response speed (10 s) (Fig. 4e). It can be seen that the response speed increases with the increase of concentration (Fig. S6 in Supporting information), but a longer response time is required at low concentration, mainly because the low reaction frequency at low concentration leads to slow rate of resistance change. With the increase of concentration, the recovery time increases gradually, which can be attributed to more benzene molecules adsorbed on the material surface, and the desorption takes longer time due to the stronger binding capacity between benzene and sensitive materials. In addition, the produced H_2O molecules can form water film on the surface of sensitive materials to restrict the desorption behavior [47], and thus the recovery time is relative longer.

In the sensing process, O_2 molecules are adsorbed on the surface of the materials, and it can obtain electrons from the interior of the S/mWO$_3$-*X* materials to form electron depletion layer (Scheme 2). After reacting with benzene molecules, it can release electrons back to the interior of the S/mWO$_3$-*X* materials to reduce the resistance (Eqs. 1–4) [48–51].

$$O_2(g) \rightarrow O_2(ads) \quad (1)$$

$$O_2(ads) + e^- \rightarrow O_2^-(ads) \quad (2)$$

$$O_2^-(ads) + e^- \rightarrow 2O^- \quad (3)$$

$$15O^-(ads) + C_6H_6 \rightarrow 6CO_2 + 3H_2O + 15e^- \quad (4)$$

It can be seen from XPS spectra that under the conditions of S doping and high-temperature S losing, the internal defects and surface adsorbed oxygen content will increase significantly, which will promote the catalytic reaction between benzene molecules and S/mWO$_3$-*X* materials [52]. The improvement of performance is mainly determined by the reaction between the adsorbed oxygen species and the target gas (Eq. 5):

$$R = R_a/R_g = aC^b + 1 \quad (5)$$

The logarithm of both sides of Eq. 5 is plotted simultaneously (Fig. 5), in which *a* in the equation is related to the materials, target gas and working temperature, and the oxygen species state on the surface is related to *b*. According to the relevant literature reports, the range of *b* value is usually between 0.25 and 1. When the parameter is closer to 1, the surface oxygen species mainly exist in the form of O^-, which can promote the surface catalytic reaction. On the contrary, the existence in the form of O^{2-} will be not conducive to the improvement of response value. After S element doping, the value of *b* gradually increases and reaches the maximum at S/mWO$_3$-5. It shows that the active oxygen (O^-) content on the surface of S/mWO$_3$-5 is the highest, which helps to improve the sensing response, and it is consistent with the experimental results [53–55]. Therefore, after the introduction of S atom, more highly active O^- will be obtained on the material surface to promote the surface catalytic reaction, which can improve the gas sensing performance.

In conclusion, a facile and straightforward multicomponent co-assembly method was demonstrated to conveniently synthesize mesoporous S-doped crystalline WO_3 materials by using PEO-*b*-PS as the template and 4-hydroxyphenylthiophenol as sulfur source. The as-synthesized S/mWO$_3$ materials have high specific surface area (40.9–63.8 m^2/g) and uniform pore size (~18 nm). After introducing a certain amount of S elements, it can generate more oxygen vacancies and internal defects *via* local lattice distortion of WO_3 crystal, which can provide more reaction sites for enhancing benzene series sensing performance, especially for the lower working temperature (250 °C). In addition, the designed S/mWO$_3$-5 sensor exhibited optimal benzene sensing performance, including ultrahigh sensitivity toward 50 ppm benzene (R_a/R_g = 48), rapid response rate (*ca.* 10 s), excellent selectivity to benzene series and high long-term stability. Especially, it can detect ultralow benzene concentration (500 ppb), which exhibits extensive potential in multi-application fields. This method provides a new idea for the synthesis of non-metallic elements-doped SMOs sensitive materials for smart gas sensor.

Declaration of competing interest

The authors declare that they have no known competing financial interests or personal relationships that could have appeared to influence the work reported in this paper.

Acknowledgments

This work was supported by the National Natural Science Foundation of China (Nos. 22125501, U22A20152, 22105043, 52225204, 52173233), Key Basic Research Program of Science and Technology Commission of Shanghai Municipality (No. 20JC1415300), the state key laboratory of Transducer Technology of China (No. SKT2207), and the Fundamental Research Funds for the Central Universities (No. 20720220010).

Supplementary materials

Supplementary material associated with this article can be found, in the online version, at doi:10.1016/j.cclet.2023.108898.

References

[1] S. Mahajan, S. Jagtap, Appl. Mater. Today 18 (2020) 100483.
[2] L. Liu, M. Ikram, L. Ma L, et al., J. Hazard. Mater. 393 (2020) 122325.
[3] D. Zhang, J. Wu, P. Li, et al., ACS Appl. Mater. Interfaces 11 (2019) 31245–31256.
[4] T.J. Gounder, P.S.K. Khadheer, Chemosphere 277 (2021) 130237.
[5] W. Zhang, H. Ma, T. Li, et al., Chin. Chem. Lett. 33 (2022) 3726–3732.
[6] D. Wang, Y. Yin, P. Xu, et al., J. Mater. Chem. A 8 (2020) 11188–11194.
[7] Y. Zou, X. Zhou, Y. Zhu, et al., Acc. Chem. Res. 52 (2019) 714–725.
[8] H. Tian, H. Fan, J. Ma, et al., J. Hazard. Mater. 341 (2018) 102–111.
[9] X. Zhou, W. Feng, C. Wang, et al., J. Mater. Chem. A 2 (2014) 17683–17690.
[10] X. Dong, Q. Han, Y. Kang, et al., Chin. Chem. Lett. 33 (2022) 567–572.
[11] X. Yang, Y. Deng, H. Yang, et al., Adv. Sci. 10 (2023) 2204810.
[12] G. Wang, S. Yang, L. Cao, et al., Coord. Chem. Rev. 445 (2021) 214086.
[13] C. Yuan, J. Ma, Y. Zou, et al., Adv. Sci. 9 (2022) 2203594.
[14] Z. Zhang, J. Ma, Y. Deng, et al., ACS Appl. Mater. Interfaces 15 (2023) 15721–15731.
[15] S.J. Kim, S.J. Choi, J.S. Jang, et al., ACS Nano 10 (2016) 5891–5899.
[16] S.J. Kim, S.J. Choi, J.S. Jang, et al., Adv. Mater. 29 (2017) 1700737.
[17] Y. Ren, Y. Zou, Y. Liu, et al., Nat. Mater. 19 (2020) 203–211.
[18] W.T. Koo, J.H. Cha, J.W. Jung, et al., Adv. Funct. Mater. 28 (2018) 1802575.
[19] Y. Liu, R. Guo, K. Yuan, et al., Chem. Mater. 34 (2022) 2321–2332.
[20] V. Postica, J. Gröttrup, R. Adelung, et al., Adv. Funct. Mater. 27 (2017) 1604676.
[21] B. Liu, K. Li, Y. Luo, et al., Chem. Eng. J. 420 (2021) 129881.
[22] A. Shanmugasundaram, D.S. Kim, N.D. Chinh, et al., Chem. Eng. J. 421 (2021) 127740.
[23] C. Jin, J. Lian, Y. Gao, et al., ACS Sustain. Chem. Eng. 7 (2019) 13989–13998.
[24] A.V. Raghu, K.K. Karuppanan, B. Pullithadathil, Adv. Mater. Interfaces 6 (2019) 1801714.
[25] V. Parey, M.V. Jyothirmai, E.M. Kumar, et al., Carbon 143 (2019) 38–50.
[26] N. Ploysongsri, V. Vchirawongkwin, V. Ruangpornvisuti, Vacuum 187 (2021) 110140.
[27] G. Chen, L. Gan, H. Xiong, et al., Membranes 12 (2022) 77.
[28] W. Li, C. Ding, J. Li, et al., Appl. Surf. Sci. 502 (2020) 144140.
[29] N.R. Tanguy, M. Arjmand, N. Yan, Adv. Mater. Interfaces 6 (2019) 1900552.
[30] L. Xia, X. Wu, Y. Wang, et al., Small Methods 3 (2018) 1800251.
[31] L. Zhang, X. Zhu, Z. Wang, et al., RSC Adv. 9 (2019) 4422–4427.
[32] H. Fu, H. Luo, Q. Lin, et al., Chem. Eng. J. 409 (2021) 128201.
[33] S. Liu, G. Li, Y. Gao, et al., Catal. Sci. Technol. 7 (2017) 4007–4016.
[34] Z. Hong, Y. Zhen, Y. Ruan, et al., Adv. Mater. 30 (2018) e1802035.
[35] X. Chen, Z. Guo, W. Xu, et al., Adv. Funct. Mater. 21 (2011) 2049–2056.
[36] Y. Zhang, J. Zhao, H. Sun, et al., Sens. Actuator. B 266 (2018) 364–374.
[37] X. Zhou, Y. Zhu, W. Luo, et al., J. Mater. Chem. A 4 (2016) 15064–15071.
[38] J. Ma, Y. Ren, X. Zhou, et al., Adv. Funct. Mater. 28 (2017) 1705268.
[39] H. Chen, Y. Zhao, L. Shi, et al., ACS Appl. Mater. Interfaces 10 (2018) 29795–29804.
[40] T.H. Eom, S.H. Cho, J.M. Suh, et al., Small 18 (2022) 2106613.
[41] J. Deng, C. Ye, A. Cai, et al., Chem. Eng. J. 420 (2021) 129863.
[42] M.P. Suryawanshi, U.V. Ghorpade, S.W. Shin, et al., ACS Catal. 7 (2017) 8077–8089.
[43] C. Han, M. Pelaez, V. Likodimos, et al., Appl. Catal. B: Environ. 107 (2011) 77–87.
[44] T. Wagner, S. Haffer, C. Weinberger, et al., Chem. Soc. Rev. 42 (2013) 4036–4053.
[45] X. Zhou, X. Cheng, Y. Zhu, et al., Chin. Chem. Lett. 29 (2018) 405–416.
[46] Y. Zhang, Q. Yang, X. Yang, et al., Microporous Mesoporous Mater. 270 (2018) 75–81.
[47] W. Guo, Q. Zhou, J. Zhang, et al., Sens. Actuator. B 299 (2019) 126959.
[48] A. Sharma, C.S. Rout, J. Mater. Chem. A 9 (2021) 18175–18207.
[49] A. Dey, Mater. Sci. Eng. B 229 (2018) 206–217.
[50] X. Wang, R. Cao, S. Zhang, et al., J. Mater. Chem. A 5 (2017) 23999–24010.
[51] A. Yadav, P. Singh, G. Gupta, Environ. Sci. Nano 9 (2022) 40–60.
[52] D. Wang, D. Zhang, Q. Mi, Sens. Actuator. B 350 (2022) 130830.
[53] J. Bai, Y. Luo, C. Chen, et al., Sens. Actuator. B 324 (2020) 128755.
[54] R.W.J. Scott, S.M. Yang, G. Chabanis, et al., Adv. Mater. 13 (2001) 1468–1472.
[55] M. D'Arienzo, L. Armelao, C.M. Mari, et al., J. Am. Chem. Soc. 133 (2011) 5296–5304.